



TECHNICAL ARTICLE

# Effect of Solution Treatment Temperature on Microstructure, Mechanical Properties, and Corrosion Resistance of 5A Super Duplex Stainless Steel

Chenlu Liu, Aiqin Wang, Hang Wang, and Jingpei Xie

Submitted: 3 April 2022 / Revised: 29 September 2022 / Accepted: 16 October 2022 / Published online: 31 October 2022

The effect of solution temperature on the microstructure of 5A super duplex stainless steel (SDSS) was investigated by scanning electron microscopy (SEM), energy-dispersive spectrometry (EDS), and transmission electron microscope (TEM). The corrosion resistance of the samples after solution heat treatment is analyzed by chemical immersion and electrochemical test. The experimental results show that with an increasing solution temperature, the ratio of  $\alpha/\gamma$  phase is close to 1:1 at 1080 °C, demonstrating the best anti-corrosion and mechanical properties. When the temperature of solid solution is 950 °C, the content of  $\sigma$  phase is higher than the other samples, which seriously affects the mechanical properties and corrosion resistance. According to the TEM results, it is found that there is a coherent relationship between the  $\sigma$  and  $\alpha$  phases, which proves that the eutectoid reaction of the  $\alpha$  phase leads to the formation of  $\sigma$  phase.

**Keywords** 5A duplex stainless, corrosion resistance, microstructure, solution treatment

## 1. Introduction

In the super duplex stainless steel (SDSS), the amount of the ferrite ( $\alpha$ ) and austenite ( $\gamma$ ) is similar, thereby the SDSS can possess the advantages of the strength of ferrite stainless steel and the toughness of austenite stainless steel (Ref 1). Due to the excellent weldability and corrosion resistance (with a pitting resistance equivalent of over 40) of the SDSS, it plays a vital role in marine construction, oil, gas, and the chemical industries (Ref 2, 3). Nowadays, 5A SDSS with highly alloying elements has been developed and employed in high-chlorine environments such as deep-sea industry (Ref 4-6).

With the increase in solution treatment temperature, the content of ferrite increases, while the content of austenite decreases. When the two-phase ratio is close to 1:1, the mechanical properties and corrosion resistance of 5A SDSS can be enhanced (Ref 7-9). The kinds and amount of the alloying elements, as well as the solution treatment temperature, are the main factors, which will affect the two-phase ratio (Ref 10). The improper heat treatment process will cause the formation of harmful phases such as the intermetallic compounds precipi-

tated along grain boundaries, which will reduce the corrosion resistance and mechanical properties of materials (Ref 11-13).

The morphologies of the sigma ( $\sigma$ ) phase were researched (Ref 14), and it was found that when heat treatment temperature was 920 °C, the  $\sigma$  showed lacy microstructure, while it showed block-shape after treated at 980 °C. Liu et al. (Ref 15) combined the electrochemical with impacting toughness and verified that the Cr-rich carbides decrease the impact toughness. In addition, Falodun et al. (Ref 16) found that the hot-rolled sample had higher mechanical properties and wear resistance than the solid solution sample. Solution treatment changes the distribution of the alloying elements and the ratio of the two phases, so that the two phases produce a chemical gradient to form a galvanic cell (Ref 17). Luo et al. (Ref 18) have found that pits initiation sites occur in the  $\gamma$  phase near the  $\gamma/\alpha$  boundaries or at the inclusions. And it has been demonstrated that the non-diffusible phase change occurred during cold processing is also one of the reasons for the decreasing corrosion resistance of materials (Ref 19). Furthermore, Luca Pezzato (Ref 20) have reported that the nitride precipitated at grain boundaries would also affect the corrosion resistance and reduce the toughness of the duplex stainless steel (DSS).

The melting process of 5A SDSS is complex. The scholars have paid a lot of attention on the microstructure and precipitate of DSS, while there are just a few works reported about its mechanical properties. In this case, we used a relatively mature internal controlled composition and smelting process to meet the requirements of ASME-SA995 standards. What's more, the content of P and S in samples is lower than the standards, so the mechanical properties of samples are better. To face the industrial need, it is necessary to optimize the microstructure of the material, which requires proper heat treatment, thereby improving the performance. This study aimed to evaluate the microstructure changes of as-cast 5A SDSS after solution treatment and investigate the effect of solution treatment temperature on its mechanical properties and corrosion resistance.

**Chenlu Liu, Aiqin Wang, and Jingpei Xie**, College of Materials Science and Engineering, Henan University of Science and Technology, Luoyang 471023, People's Republic of China; and Provincial and Ministerial Co-Construction of Collaborative Innovation Center for Non-Ferrous Metal New Materials and Advanced Processing Technology, Luoyang 471023, People's Republic of China; **Hang Wang**, Luoyang CITIC HIC Casting & Forging Co., Ltd, Luoyang 471023, People's Republic of China. Contact e-mail: aiqin\_wang888@163.com.

## 2. Experimental Procedure

### 2.1 Experimental Materials and Methods

The chemical composition (in mass %) of 5A SDSS was 0.03 C, 25.32 Cr, 6.7 Ni, 4.15 Mo, 0.26 N, 0.015 Si, 0.032 P and the balance Fe. The sample was smelted in a medium frequency induction furnace, molded with alkali-phenolic resin sand, and deoxidized with compound deoxidize. Kiel test block was used as a casting test block. Solid solution treatment was carried out in the XWL-13-5Y high-temperature box resistance furnace. Firstly, the samples were heated up to 790 °C and hold for 2 h, and then heat treated at 1130 °C for 2 h. Subsequently, the samples were cooled to 950, 1000, 1040, 1060, 1080, and 1100 °C and hold for 2 h, respectively. At last, the samples were quenched with water to room temperature.

### 2.2 Performance Measurements and Microstructure Characterization

X-ray diffraction (XRD) patterns were collected using an ADVANCE D8 diffractometer equipped operating with Cu K $\alpha$  radiation with a step speed of 1° s<sup>-1</sup>. JB-W300 semi-automatic pendulum impact testing machine was used to test the impact performance. The size of the Charpy V-notch impact samples was 10 × 10 × 55 mm<sup>3</sup> and they were tested at -46 °C. The tensile properties at room temperature were detected on a Shimadzuag-1250kN precision universal tester. The size of the tensile samples is shown in Fig. 1. The impact and tensile results were average values of three samples for each tested condition.

Immersion and electrochemical tests were used to investigate the material's corrosion resistance. Following the GB/T 17897-1999, a chemical immersion pitting test was performed in 0.16 wt.% HCl + 6 wt.% FeCl<sub>3</sub> solutions at 50 ± 1 °C for 24 h. The surface area and weight of the samples were measured before testing. After the test, each sample was rinsed with alcohol and cleaned with an ultrasonic cleaner. It was then dried in a drying oven and weighed. CHI1660 electrochemical workstation with a three electrodes system was employed to carry out electrochemical tests at room temperature. The surface area of sample was about 1 cm<sup>2</sup>, which was used as the working electrode. The saturated calomel electrode (SCE) was regarded as the reference electrode, and the graphite electrode was served as the counter electrodes. The samples with a size of 10 × 10 × 5 mm<sup>3</sup> were prepared and sealed by phenolic epoxy resin. The exposed area was sanded with SiC papers up to a grit of 800 mesh and then mechanically polished using diamond pastes (2.5 μm). The same polishing and cleaning procedures were carried out for all samples. The electrochemical tests were operated in 3.5 wt.% NaCl solution. Before the test, the samples were immersed in the solution for 40 min to achieve a stable open circuit potential (OCP). The

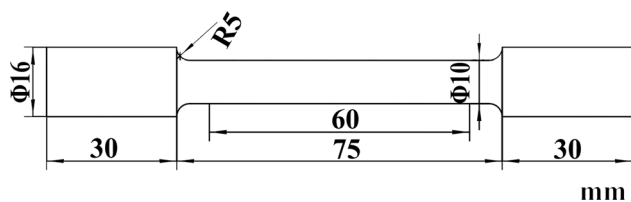


Fig. 1 Dimensions of tensile specimen in the test

polarization curves were measured at a scan rate of 0.33 mV·s<sup>-1</sup>, and the scanning voltage ranged from -0.5 V + 1.25 V. Corrosion morphologies were observed on a JSW-5610 scanning electron microscope (SEM).

The samples were ground, polished, and then etched by etchant (1 g K<sub>2</sub>S<sub>2</sub>O<sub>5</sub> + 20 mL HCl + 100 mL H<sub>2</sub>O). The phase fractions were analyzed using an image analyzer (Image-Pro Plus 6.0). Ten pictures were selected to calculate the two-phase ratio for all samples. SEM was used to observe the impact fracture morphologies of the samples. The microstructures of the samples were observed and analyzed using a transmission electron microscope (TEM) of JEM-2100. The thin foils were prepared by twin-jet electropolishing in a chemical solution of 10% (volume fraction) perchloric acid and 90% (volume fraction) glacial acetic acid at -20 °C and 50 V.

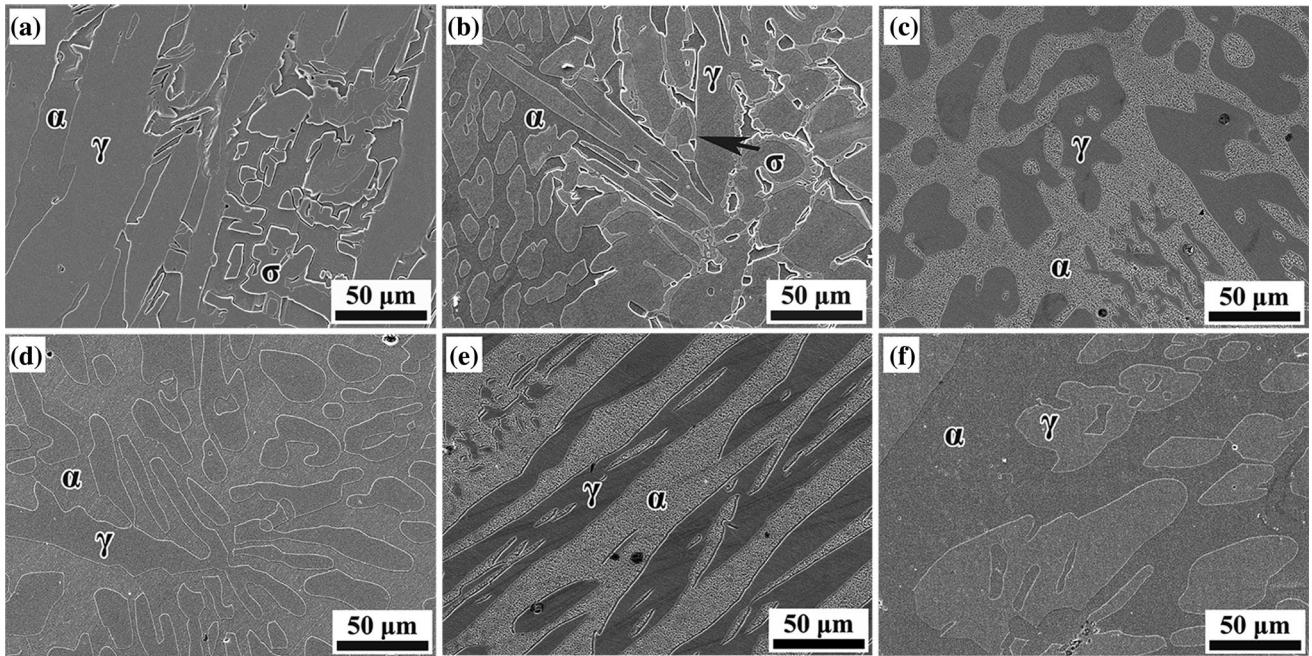
## 3. Result

### 3.1 Microstructure of 5A Duplex Stainless Steel

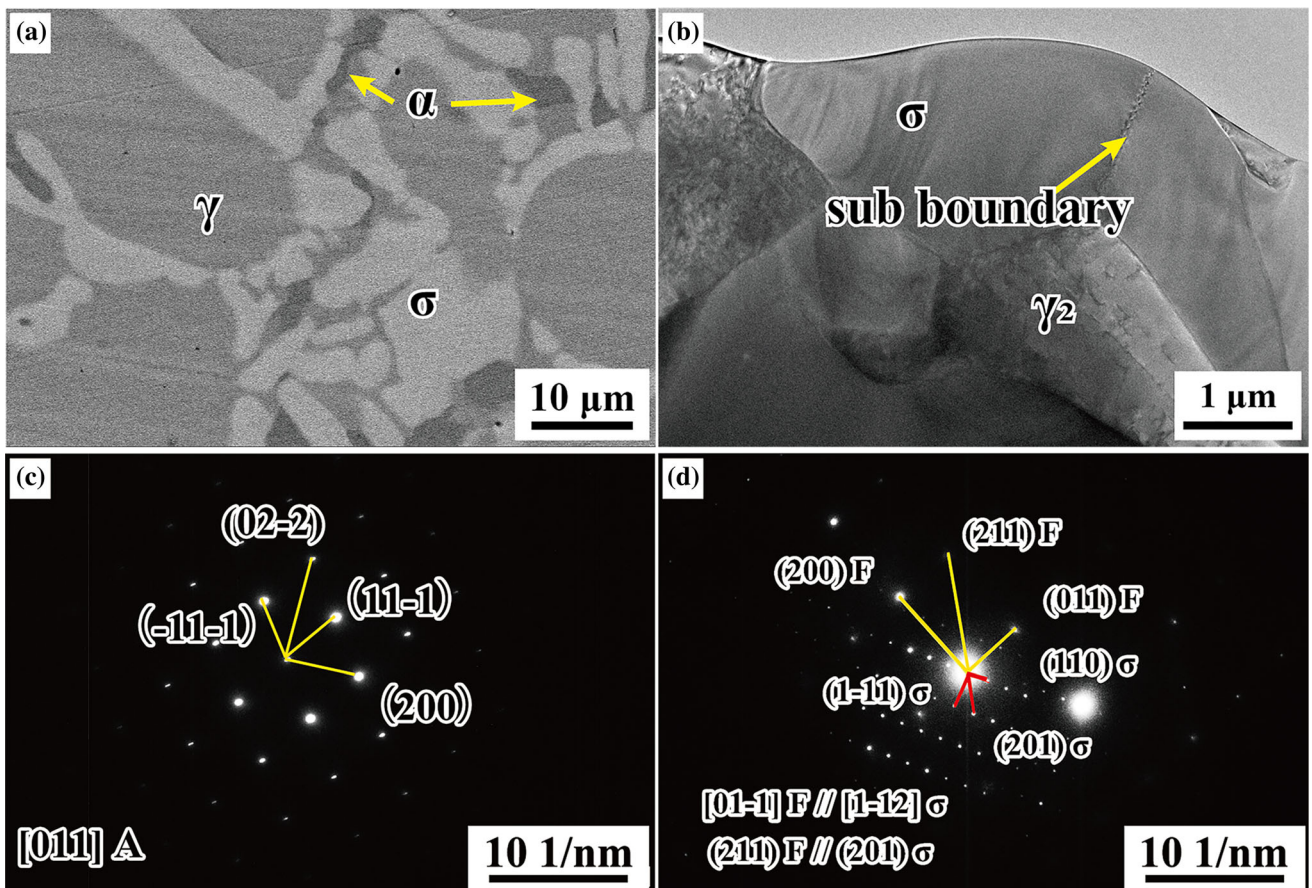
Figure 2 shows the structure of samples treated at different solution temperatures. As can be seen from Fig. 2, the eutectoid reaction,  $\alpha \rightarrow \gamma_2 + \sigma$ , occurs during solution heat treatment at 950 °C, and the blocky  $\sigma$  phase precipitated between the  $\alpha$  and  $\gamma$  phase. When the solid solution temperature reaches 1000 °C, just a little  $\sigma$  phase can be observed in the phase boundaries. As the solid solution temperature exceeds 1000 °C, the microstructure of the two phases changes. With the increase in temperature, the area of the ferrite rises, and new austenite is precipitated at the ferrite matrix.

Figure 3 exhibits the morphologies of the  $\sigma$  phase analyzed by BSE and TEM. The brightest phase in Fig. 3(a) is the precipitated  $\sigma$  phase at the boundary between the light gray  $\gamma$  phase and the dark gray  $\alpha$  phase. Figure 3(c) and (d) shows the diffraction patterns of different phases in Fig. 3(b), which are  $\gamma$ ,  $\alpha$ , and  $\sigma$  phases, respectively. It can be seen from Fig. 3(b) that the  $\sigma$  phase precipitated from the matrix and grew up along with the formation of sub-grain boundaries. It was found that (211) F is parallel to (201)  $\sigma$ , and [01-1] F is parallel to [1-12]  $\sigma$ . According to calculation results, the lattice misfit between the  $\alpha$  and  $\sigma$  is 4.37%, indicating that the phase boundary of  $\alpha$  and  $\sigma$  is parallel and coherent. Therefore, it is proved that  $\sigma$  phase is formed by the eutectoid decomposition of  $\alpha$  phase. The precipitate changes the element distribution of the matrix, which significantly affects the properties of samples. Table 1 shows the chemical composition (in mass%) of different phases in the samples treated at 950 °C. The element contents of Cr and Mo in the  $\alpha$  phase are higher than those in the  $\gamma$  phase, while the content of Ni is lower than the  $\gamma$  phase.

Figure 4 shows XRD patterns of samples treated at various solution temperatures. It can be seen from Fig. 4 that there is a low  $\sigma$  phase diffraction peak when the sample is solution treated at 950 °C. The ratio of the two phases is generally seen as a significant factor for the mechanical properties (Ref 21). According to the measurement of image J software, the content of the  $\sigma$  phase reaches 28.68% in the sample solution treated at 950 °C. As shown in Fig. 4, the ratio of the two phases has gradually increased with the increasing temperature, and it even reaches approximately 1:1 when the solid solution temperature exceeds 1060 °C. The overall reactions for the ferrite can be considered as follows: One is the eutectoid decomposition, and



**Fig. 2** The SEM image of the microstructure of the 5A SDSS solution treated at different temperatures (a) 950 °C; (b) 1000 °C; (c) 1040 °C; (d) 1060 °C; (e) 1080 °C; (f) 1100 °C



**Fig. 3** (a) BSE image of specimen solution treated at 950 °C and Transmission electron microscopy (TEM) micrograph of duplex stainless steel; (b) morphology of precipitates; (c) diffraction pattern of the  $\gamma_2$  phase; (d) diffraction pattern of  $\alpha + \sigma$  phase

another is the two-phase transformation. When solution treatment temperature is above 1000 °C, the ferrite content changes only relate to the phase transition of  $\gamma$  and  $\alpha$ .  $\gamma$  converts to  $\alpha$  as the temperature rises. Meanwhile, when the temperature is above 1060 °C, the transition amount is limited as the reported work (Ref 22).

### 3.2 The Mechanical Properties of 5A Duplex Stainless Steel

The mechanical properties of 5A SDSS solution treated at different temperatures are shown in Fig. 5. As can be seen from

**Table 1 Chemical compositions of various microstructures in the tested steel solution at 950 °C, wt.%**

	Cr	Ni	Mo	Si	Fe
$\sigma$	30.34	4.53	8.18	0.75	56.20
$\alpha$	25.84	4.85	4.28	0.62	64.41
$\gamma$	22.40	7.40	3.60	0.55	66.15

Fig. 5, the mechanical properties of sample solution treated at 950 °C are low, as the precipitation of the  $\sigma$  phase has a damaging effect on the toughness. The elongation and percentage reduction in area are within 10 J and 5%, which cannot meet the need of technical requirement. Besides, the strength and impact toughness of the 5A SDSS are also influenced by the precipitation of  $\sigma$  phase. And the average impact energy of the sample at -46 °C is only 17.7 J. There is no doubt that the terrible properties are related to the distribution and proportion of intermetallic precipitates. The  $\sigma$  phase is brittle and can be easily fractured when impact occurs (Ref 23). And the  $\sigma$  phase belongs to intermetallic phase and presents a tetragonal structure with higher hardness. It is harmful to the stability of the matrix and leads to the crack propagation easily. When the sample is solution treated at 1000 °C, there still exists  $\sigma$  phase, resulting in the yield strength lower than 500 MPa, which also cannot meet the practical requirements. The tensile strength is basically consistent with the changes in the impact performance.

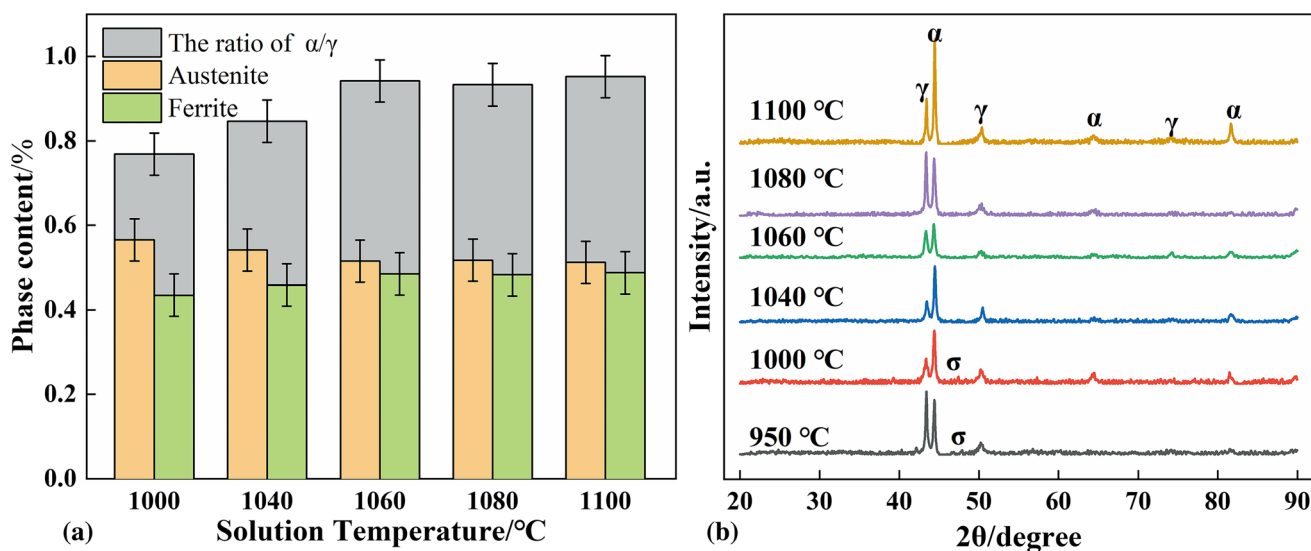


**Fig. 4** (a) the relationship between solution treatment temperature and phase ratio  $\alpha/\gamma$ , (b) XRD pattern

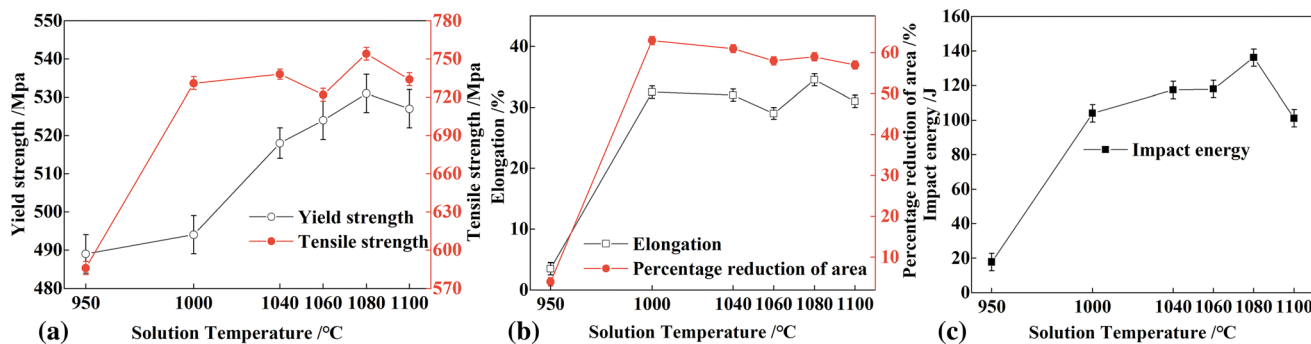


**Fig. 5** Mechanical properties of 5A SDSS vary with different solution temperatures

### 3.3 Fracture Morphology Analysis

The fracture morphologies of the samples solution treated at different temperatures are presented in Fig. 6. The results show that the fracture behavior is changed from the manner of intergranular brittle fracture to ductile fracture with many dimples. When the temperature of solution treatment is 950 °C, the fracture mechanism is an intergranular fracture with clear cracks along the phase boundaries. As can be seen from Fig. 6(a), the shedding of  $\sigma$  phase causes the production of cracks, and the cracks are grown along the precipitate. After being solution treated at 1040 °C, the fracture surface of the sample is mainly composed of tear ridges, dimples and inclusions. As shown in Fig. 6(b), the inclusions are the sources of dimples. When the sample is solution treated at 1080 °C, the fracture mechanism belongs to ductile fracture. Compared with the sample solution treated at 1040 °C, the

sample treated at 1080 °C has larger dimples, less tearing edges, and less inclusions.

### 3.4 Effect of Solution Temperature on Pitting Corrosion

**3.4.1 Chemical Immersion Test.** Figure 7 shows the effect of solution temperature on the corrosion rate of the 5A SDSS. As shown in Fig. 7, with the increasing temperature of the solution treatment, the corrosion rate of 5A SDSS firstly decreases and then increases. When the sample is solution treated at 950 °C, the corrosion rate reaches the maximum, 7.7 g/(m<sup>2</sup>·h). When the solid solution temperature ranges from 1000-1080 °C, the corrosion rate declines to around 1 g/(m<sup>2</sup>·h) and achieves the lowest value of 0.6 g/(m<sup>2</sup>·h) at 1080 °C. When the sample is solution treated at 1100 °C, the corrosion rate increases due to the presence of nitrides.

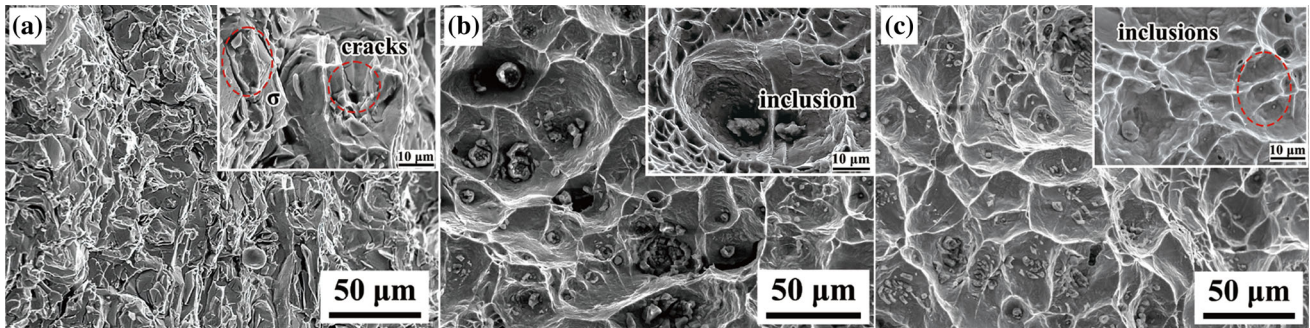


**Fig. 6** SEM micrographs showing morphology of the impact fracture for the 5A SDSS solution treated at different temperatures (a) 950 °C; (b) 1040 °C; (c) 1080 °C

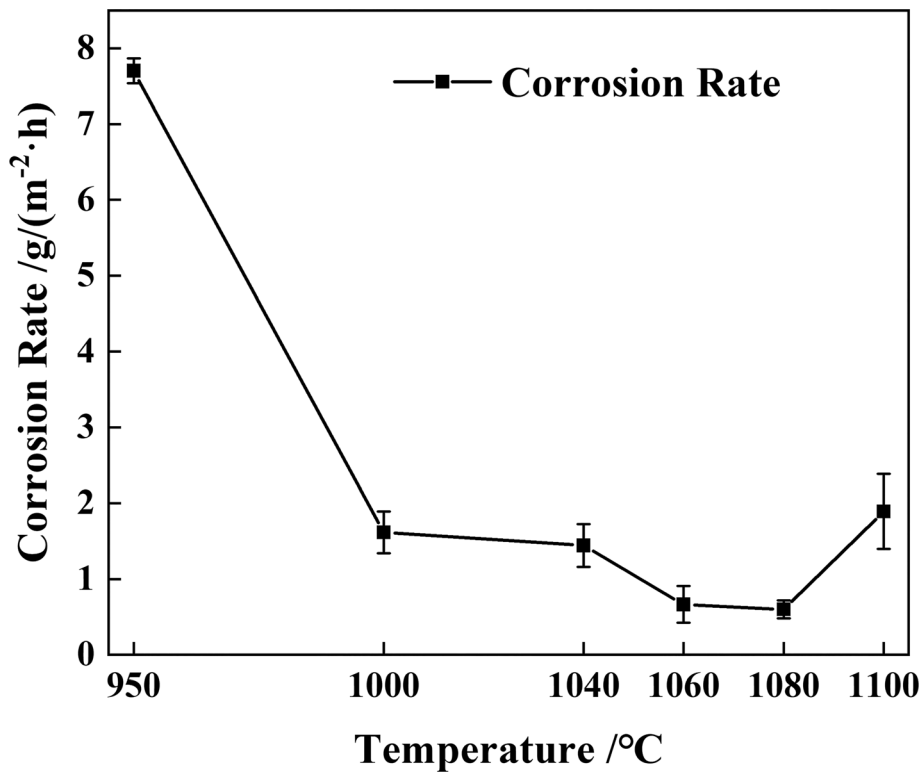


**Fig. 7** Effect of solution temperature on the corrosion rate of 5A SDSS

**3.4.2 Polarization Behavior.** Figure 8(a) shows the polarization curves of the samples solution treated at different temperatures. The cathodic polarization of them are shows the same trend, similar anodic polarization behavior, and wide passivation area, indicating good corrosion resistance. Figure 8(b) shows the self-corrosion potential ( $E_{\text{corr}}$ ), pitting potential ( $E_{\text{pit}}$ ), passivation region, and passivation current density ( $I_{\text{pass}}$ ).  $E_{\text{pit}}$  is defined as the potential, at which the current density sharply increases (Ref 24). Due to the existence of the passivation region,  $I_{\text{pass}}$  is used to evaluate the corrosion resistance (Ref 25). As the temperatures of solution treatment increased, the passivation region of the samples becomes large, and the fluctuation of the curve decreases, indicating that the pitting susceptibility of the material is reduced. When the sample is solution treated at 950 °C, the passivation region is the lowest, and the  $I_{\text{pass}}$  is higher than other samples.

Meanwhile, the  $I_{\text{pass}}$  of the sample solution treated at 1080 °C is the lowest, indicating that its passivation film has the best stability. There are two passivation zones between the self-corrosion and the pitting potential of the samples solution treated at 1060 and 1080 °C, respectively, representing the dissolution of different phases (Ref 26).

**3.4.3 Pitting Morphology.** Figure 9 shows the surface morphologies of solution samples treated at different temperatures after the electrochemical test. It can be seen from Fig. 9(a) that when the solid solution temperature is 950 °C, some corrosion gullies appear around the  $\sigma$  phase. It is because that the  $\sigma$  phase has a higher potential than the matrix, resulting in the dissolution of the matrix. When the sample is solution treated at 1000 °C, the corrosion-sensitive inclusions may cause the corrosion pits generated at the boundaries between the  $\alpha$  and  $\gamma$  phases. The pits inside the ferrite are related to the

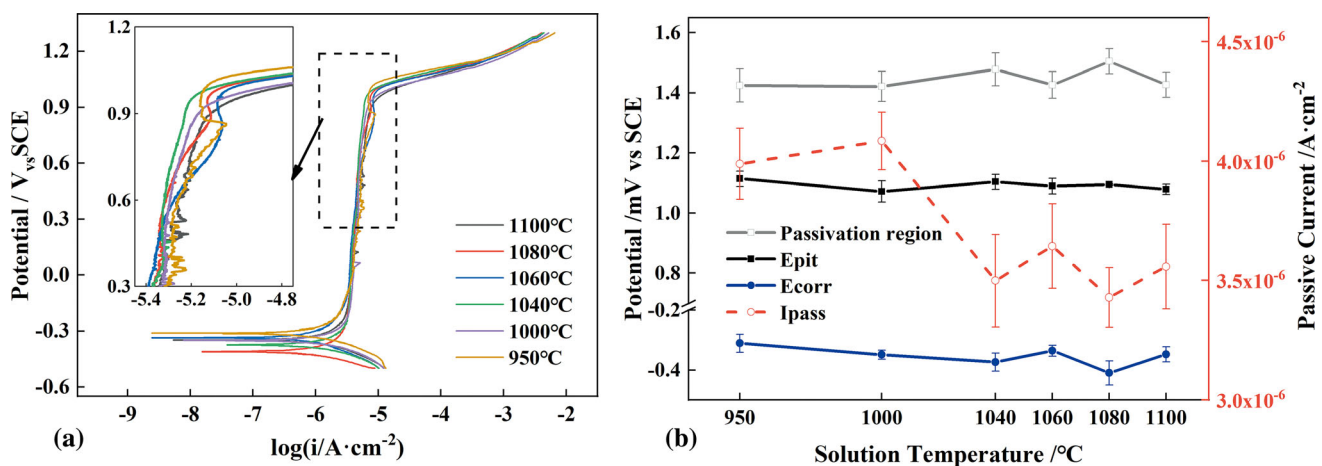


Fig. 8 Potentiodynamic polarization curves of 5A SDSS in 3.5% NaCl solution after treatment at different temperatures

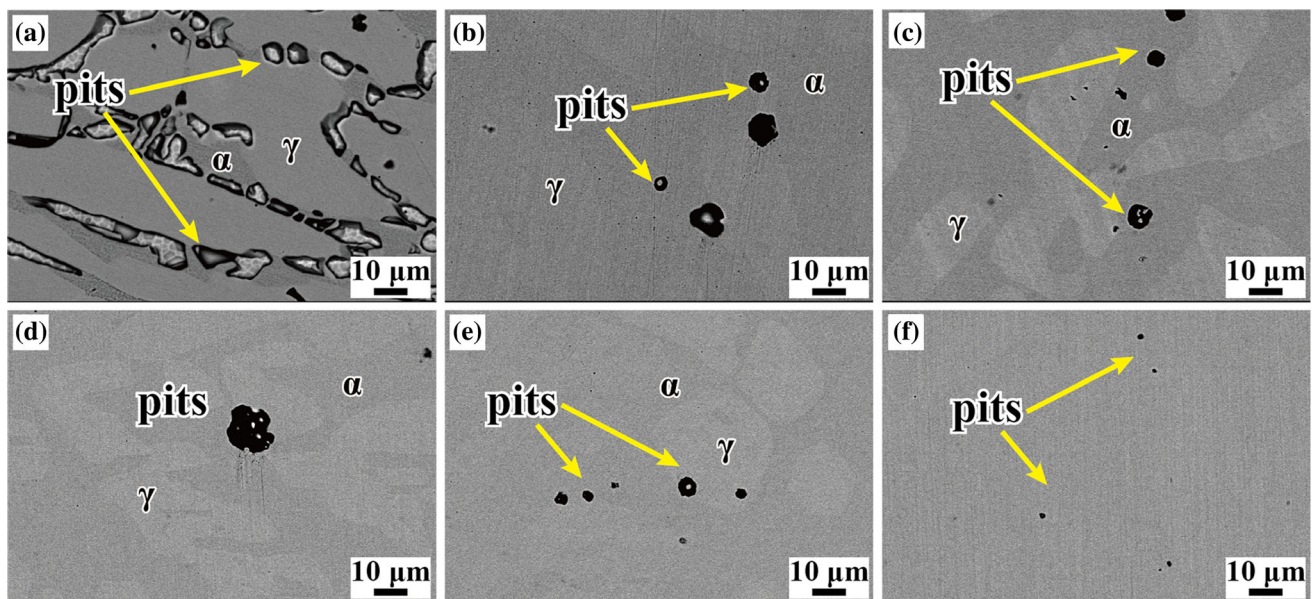


Fig. 9 The SEM image of the pitting morphology of 5A SDSS solution treated at different temperatures (a) 950 °C; (b) 1000 °C; (c) 1040 °C; (d) 1060 °C; (e) 1080 °C; (f) 1100 °C

nitrides present (Ref 27). With the increase in solution temperature from 1040-1100 °C, the pitting mainly occurs in the  $\alpha$  phase, the size of pits decreases, and the number of pits increases.

## 4. Discussion

The effect of solution temperature on the microstructure is mainly reflected in the change of the  $\gamma$  and  $\alpha$  phases ratio. Besides, it also affects the distribution of elements, as well as the precipitation and dissolution of the intermetallic compounds (Ref 28, 29). When the sample is solution treated at 950 °C, the eutectoid reaction occurs,  $\alpha$  phase is decomposed to form  $\sigma$  and  $\gamma_2$  phases. The eutectoid reaction can be proved by the interface relationship between the  $\alpha$  and  $\sigma$  phase. The  $\sigma$  phase precipitates along the two-phase boundaries, redistributing alloying elements (Table 1). When the material suffers an impact, microcracks first take place in the  $\sigma$  phase, continue to extend, and eventually cause the fracture. The  $\sigma$  phase changes the propagating direction of the cracks and results in the fractured way changing from transgranular rupture to intergranular fracture. Impact toughness can reflect the resistance of the samples to deformation and fracture. At the solution temperature of 1000 °C, a small amount of  $\sigma$  phase in the SDSS reduces its yield strength, but it still has high tensile strength and impact toughness. In this case, the content of the  $\sigma$  phase is low, and the  $\alpha$  and  $\gamma$  phases are the main phases to undergo the stress. Thereby, it shows excellent plasticity, including the high tensile strength and elongation of materials. With the rising solution temperature, the content of ferrite increases, while metastable austenite precipitation decreases. When the solid solution temperature exceeds 1000 °C, the plastic toughness of the material decreases with the increasing amount of ferrite. Guo et al. (Ref 30) have reported that the strength of the material is related to the content of the metastable austenite in the material. Lacerda et al. (Ref 27) found that nitrides within ferrite did not change the tensile fracture mechanism. According to the research (Ref 31), the unevenly distributed inclusions make the stress concentrated, which is harmful to the impact property of the material. When the sample is solution treated at 1080 °C, the microstructure distribution of the two phases is uniform, and the precipitate is relatively small and uniform. Figure 5 shows that the sample solution treated at 1080 °C owns good mechanical properties.

Pitting corrosion is one of the most harmful corrosion forms of DSS. It is the initial site of corrosion crack, which will cause substantial economic losses. At present, the chemical immersion method and the potentiodynamic polarization test are used to evaluate the pitting corrosion. The  $E_{\text{corr}}$  represents the corrosion resistance tendency of the material, and the  $I_{\text{pass}}$  represents the actual corrosion rate of the material when passivation occurs. As seen from Fig. 8, all samples have large passivation areas, reflecting passivation film corrosion and the “rehealing” phenomenon. When the solid solution temperature increases from 1040-1100 °C, the passive region increases, and the instability of the passivation film increases, indicating that the content of the ferritic is increased during the solution treatment (Ref 26). Combined with the immersion and electrochemical tests, the sample treated at 1080 °C exhibits good corrosion resistance. Sample solutions treated at 950 and 1000 °C have a higher  $I_{\text{pass}}$ , indicating a higher corrosion rate.

It is because that galvanic corrosion occurs between the  $\sigma$  phase with high alloy content and the surrounding matrix, which increases the corrosion rate. Especially, the sample solution treated at 950 °C has a high corrosion rate and a narrow passivation region, reflecting poor corrosion resistance. The  $\sigma$  phase is the Cr- and Mo- rich phase formed by the eutectoid decomposition of ferrite, increasing the sample’s passive current (Ref 24). The precipitation of the  $\sigma$  phase results in low content of the alloying element in the matrix, affecting the material’s corrosion resistance (Ref 12, 32). When the matrix of the  $\sigma$  phase dissolves, part of the  $\sigma$  phase may fall off, which is also one reason of the high corrosion rate in the sample solution treated at 950 °C. However, when the solid solution temperature is 1040-1100 °C, the two-phase ratio, corrosion rate, and passivation region are similar. Moreover, the distribution and size of the corrosion pits are similar as the inclusions in the impact fracture. It could be assumed that the precipitate is nitride (Ref 27). Kang et al. (Ref 21) found that ferrite became the prime site for pit nucleation by destroying the passivation film around the precipitation. However, Zhu et al. (Ref 9) found that pits mainly exist in austenite. The different locations of pits are related to the organization of the material. With the rapid cooling at high temperatures, numerous  $\text{Cr}_2\text{N}$  phase precipitates in ferrite grains due to the combination of supersaturated N and Cr (Ref 33). Therefore, homogenous pits mainly occurred in ferrite grains.

## 5. Conclusion

The microstructure and properties of 5A SDSS solution treated at different temperatures have been investigated in this work. The results can be summarized as follows:

1. When the solid solution temperature is 950 °C, it is found that (211) F is parallel to (201)  $\sigma$  and [01-1] F is parallel to [1-12]  $\sigma$ . In addition, there is a coherent interface between the  $\alpha$  and  $\sigma$  phases with a lattice mismatch ratio of 4.3%, indicating that the ferrite decomposes to form the  $\sigma$  phase.
2. When the solution temperature is as low as 950 °C, the content of  $\sigma$  phase is higher than the other samples. The  $\sigma$  phase is brittle particles, which are regarded as the source of initial cracks, reducing the mechanical property. Besides, the precipitation of the  $\sigma$  phase makes Cr-depleted areas appear in the matrix, increasing the corrosion rate of the sample, thereby decreasing its corrosion resistance properties.
3. When the temperature of solution treated is increased from 1040-1100 °C, samples have similar two-phase ratio, corrosion rate and passivation region. Especially, the sample solution treated at 1080 °C has the best mechanical and pitting corrosion resistance.

## Acknowledgments

This research was funded by the Major Science and Technology Program of Luoyang, China (grant no. 2101005A) and Provincial and Ministerial Co-construction of Collaborative Innovation Cen-

## References

1. S. Patra, A. Agrawal, A. Mandal, and A.S. Podder, Characteristics and Manufacturability of Duplex Stainless Steel: A Review, *Trans. Indian Inst. Metal.*, 2021, **74**(5), p 1089–1098. <https://doi.org/10.1007/s12666-021-02278-7>
2. G.A. Caetano, T.B. Gonoring, L.M. Coelho, T. de Sousa Luz, J.L. Rossi, and M.T.D. Orlando, Mechanical Properties Study of a Duplex Stainless Steel Weld Using Physical Simulation and Work Hardening Models, *J. Mater. Eng. Perform.*, 2022, **31**(1), p 113–127. <https://doi.org/10.1007/s11665-021-06155-8>
3. L. He, Y. Guo, X. Wu, Y. Jiang, and J. Li, Effect of Solution Annealing Temperature on Pitting Behavior of Duplex Stainless Steel 2204 in Chloride Solutions, *J. Iron Steel Res. Int.*, 2016, **23**(4), p 357–363. [https://doi.org/10.1016/s1006-706x\(16\)30057-7](https://doi.org/10.1016/s1006-706x(16)30057-7)
4. S. Vongsilathai, A.W. Lothongkum, and G. Lothongkum, Corrosion Behavior of a New 25Cr-3Ni-7Mn-0.66 N Duplex Stainless Steel in Artificial Seawater, *Mater. Test.*, 2021, **63**(6), p 505–511. <https://doi.org/10.1515/mt-2020-0086>
5. H. Zhong, X. Chen, Y. Liu, Z. Wei, H. Yu, and Q. Zhai, Influences of Superheat and Cooling Intensity on Macrostructure and Macrosegregation of Duplex Stainless Steel Studied by Thermal Simulation, *J. Iron Steel Res. Int.*, 2021, **28**, p 1125–1132. <https://doi.org/10.1007/s42243-021-00592-4>
6. Z. Zhang, H. Zhao, H. Zhang, J. Hu, and J. Jin, Microstructure Evolution and Pitting Corrosion Behavior of UNS S32750 Super Duplex Stainless Steel Welds after Short-Time Heat Treatment, *Corros. Sci.*, 2017, **121**, p 22–31. <https://doi.org/10.1016/j.corsci.2017.02.006>
7. A.F. Ciuffini, S. Barella, C. Di Cecca, A. Gruttadauria, C. Mapelli, and D. Mombelli, Isothermal Austenite-Ferrite Phase Transformations and Microstructural Evolution during Annealing in Super Duplex Stainless Steels, *Metal*, 2017, **7**(9), p 368. <https://doi.org/10.3390/met7090368>
8. S.S.M. Tavares, J.M. Pardal, E. Ponzo, A. Loureiro, and J.A. de Souza, Influence of Microstructure on the Corrosion Resistance of Hyperduplex Stainless Steel, *Mater. Corros.*, 2010, **64**(4), p 313–317. <https://doi.org/10.1002/maco.200905386>
9. M. Zhu, Q. Zhang, Y.F. Yuan, S.Y. Guo, and Y.B. Chen, Study on the Microstructure and Alternating Current Corrosion Behavior of SAF2507 Super-Duplex Stainless Steel in 3.5%NaCl Solution, *J. Mater. Eng. Perform.*, 2020, **29**(2), p 1366–1374. <https://doi.org/10.1007/s11665-020-04624-0>
10. X. Liu, C. Zhang, J. Li, W. Chen, Y. Zheng, H. Li, and P. Han, Effect of Solution Annealing on Microstructure Evolution and Pitting Corrosion Resistance of SAF2906 Super Duplex Stainless Steel, *Steel Res. Int.*, 2017, **88**(11), p 1700023. <https://doi.org/10.1002/srin.201700023>
11. G.C.L.D. Freitas, G.S. da Fonseca, L.P. Moreira, and D.N.F. Leite, Phase Transformations of the Duplex Stainless Steel UNS S31803 under Non-Isothermal Conditions, *J. Mater. Res. Technol.*, 2021, **11**, p 1847–1851. <https://doi.org/10.1016/j.jmrt.2021.02.008>
12. M. Djama, D. Saidi, A. Kadri, N. Kherrouba, B. Mehdi, S. Mathieu, T. Schweitzer, and I. Brahim, Correlation Between the Pitting Potential Evolution and  $\sigma$  Phase Precipitation Kinetics in the 2205 Duplex Stainless Steel, *J. Mater. Eng. Perform.*, 2018, **27**(8), p 3911–3919. <https://doi.org/10.1007/s11665-018-3482-8>
13. D.M. Fellicia, B.A. Sutarsis, D. Kurniawan, A.P. Wulanari, and A.T. Wibisono, Study of Sigma Phase in Duplex SAF 2507, *IOP Conf. Ser. Mater. Sci. Eng.*, 2017 <https://doi.org/10.1088/1757-899X/2021/012039>
14. M. Martins and L.C. Casteletti, Sigma Phase Morphologies in Cast and Aged Super Duplex Stainless Steel, *Mater. Charact.*, 2009, **60**(8), p 792–795. <https://doi.org/10.1016/j.matchar.2009.01.005>
15. Z. Liu, Z. Gao, C. Lv, C. Zhang, and W. Hu, Research on the Correlation between Impact Toughness and Corrosion Performance of Cr13 Super Martensitic Stainless Steel under Deferent Tempering Condition, *Mater. Lett.*, 2021, **283**, p 128791. <https://doi.org/10.1016/j.matlet.2020.128791>
16. O.E. Falodun, E.B. Mtsweni, S.R. Oke, and P.A. Olubambi, Influence of Solution Heat Treatment on Microstructure and Mechanical Properties of a Hot-Rolled 2205 Duplex Stainless Steel, *J. Mater. Eng. Perform.*, 2021, **30**, p 7185–7194. <https://doi.org/10.1007/s11665-021-05904-z>
17. H.Y. Ha, M.H. Jang, T.H. Lee, and J. Moon, Interpretation of the Relation between Ferrite Fraction and Pitting Corrosion Resistance of Commercial 2205 Duplex Stainless Steel, *Corros. Sci.*, 2014, **89**, p 154–162. <https://doi.org/10.1016/j.corsci.2014.08.021>
18. H. Luo, C.F. Dong, X.G. Li, and K. Xiao, The Electrochemical Behaviour of 2205 Duplex Stainless Steel in Alkaline Solutions with Different PH in the Presence of Chloride, *Electrochim Acta*, 2012, **64**, p 211–220. <https://doi.org/10.1016/j.electacta.2012.01.025>
19. M. Breda, L. Pezzato, M. Pizzo, and I. Calliari, Effect of Cold Rolling on Pitting Resistance in Duplex Stainless Steels, *Metall. Ital.*, 2014, **2014**(6), p 15–19
20. L. Pezzato, M. Lago, K. Brunelli, M. Breda, and I. Calliari, Effect of the Heat Treatment on the Corrosion Resistance of Duplex Stainless Steels, *J. Mater. Eng. Perform.*, 2018, **27**(8), p 3859–3868. <https://doi.org/10.1007/s11665-018-3408-5>
21. D.H. Kang and H.W. Lee, Study of the Correlation between Pitting Corrosion and the Component Ratio of the Dual Phase in Duplex Stainless Steel Welds, *Corros. Sci.*, 2013, **74**, p 396–407. <https://doi.org/10.1016/j.corsci.2013.04.033>
22. Z. Zhang, H. Zhang, J. Hu, X. Qi, Y. Bian, A. Shen, P. Xu, and Y. Zhao, Microstructure Evolution and Mechanical Properties of Briefly Heat-Treated SAF 2507 Super Duplex Stainless Steel Welds, *Constr. Build. Mater.*, 2018, **168**, p 338–345. <https://doi.org/10.1016/j.conbuildmat.2018.02.143>
23. M.V. Biezma, U. Martin, P. Linhardt, J. Röss, C. Rodríguez, and D.M. Bastidas, Non-Destructive Techniques for the Detection of Sigma Phase in Duplex Stainless Steel: A Comprehensive Review, *Eng. Fail. Anal.*, 2021, **122**, p 105227. <https://doi.org/10.1016/j.engfailanal.2021.105227>
24. R. Magnabosco and N. Alonso-Falleiros, Pit Morphology and Its Relation to Microstructure of 850°C Aged Duplex Stainless Steel, *Corrosion*, 2005, **61**(2), p 130–136. <https://doi.org/10.5006/1.3278167>
25. X. Cheng, Y. Wang, X. Li, and C. Dong, Interaction between Austenite-Ferrite Phases on Passive Performance of 2205 Duplex Stainless Steel, *J. Mater. Sci.*, 2018, **34**(11), p 2140–2148. <https://doi.org/10.1016/j.jmst.2018.02.020>
26. R. Magnabosco and N. Alonso-Falleiros, Sigma Phase Formation and Polarization Response of UNS S31803 in Sulfuric Acid, *Corrosion*, 2005, **61**(8), p 807–814. <https://doi.org/10.5006/1.3278215>
27. J.C. de Lacerda, L.C. Cândido, and L.B. Godefroid, Effect of Volume Fraction of Phases and Precipitates on the Mechanical Behavior of UNS S31803 Duplex Stainless Steel, *Int. J. Fatigue*, 2015, **74**, p 81–87. <https://doi.org/10.1016/j.ijfatigue.2014.12.015>
28. J. Li, W. Shen, P. Lin, F. Wang, and Z. Yang, Effect of Solution Treatment Temperature on Microstructural Evolution, Precipitation Behavior, and Comprehensive Properties in UNS S32750 Super Duplex Stainless Steel, *Metal*, 2020, **10**(11), p 1481. <https://doi.org/10.3390/met10111481>
29. N. Llorca-Isern, H. López-Luque, I. López-Jiménez and M.V. Biezma, Identification of Sigma and Chi Phases in Duplex Stainless Steels, *Mater. Charact.*, 2016, **112**, p 20–29. <https://doi.org/10.1016/j.matchar.2015.12.004>
30. B. Guo, Q. Zhang, C. Lei, X. Guo, L. Na, X. Liu, and J. Miao, Influence of Annealing Temperature on the Strain-Hardening Behavior of a Lean Duplex Stainless Steel, *Mater. Sci. Eng. A*, 2018, **722**, p 216–224. <https://doi.org/10.1016/j.msea.2018.03.027>
31. Z. Zhang, H. Jing, L. Xu, Y. Han, and L. Zhao, Investigation on Microstructure Evolution and Properties of Duplex Stainless Steel Joint Multi-Pass Welded by Using Different Methods, *Mater. Des.*, 2016, **109**, p 670–685. <https://doi.org/10.1016/j.matdes.2016.07.110>
32. M. Sun, X. Wu, Z. Zhang, and E.-H. Han, Oxidation of 316 Stainless Steel in Supercritical Water, *Corros. Sci.*, 2009, **51**(5), p 1069–1072. <https://doi.org/10.1016/j.corsci.2009.03.008>
33. B.-H. Shin, D. Kim, S. Park, M. Hwang, J. Park, and W. Chung, Precipitation Condition and Effect of Volume Fraction on Corrosion Properties of Secondary Phase on Casted Super-Duplex Stainless Steel UNS S32750, *Anti-Corros. Methods Mater.*, 2019, **66**(1), p 61–66. <https://doi.org/10.1108/acmm-06-2018-1958>